IEEE Access
Multidisciplinary | Rapid Review | Open Access Journal

Date of publication xxxx 00, 0000, date of current version xxxx 00, 0000.

Digital Object Identifier 10.1109/ACCESS.2017.Doi Number

3D Printing of a Monolithic K/Ka-Band Dual-Circular Polarization Antenna-Feeding Network

G. Addamo[1], Member, IEEE, M. Lumia[1], F. Calignano[2], F. Paonessa[1], G. Virone[1], Senior Member, IEEE, D. Manfredi[3], L. Iuliano[2], and O. A. Peverini[1], Member, IEEE

[1]Istituto di Elettronica e di Ingegneria dell'Informazione e delle Telecomunicazioni, National Research Council of Italy, 10129 Turin, Italy
[2]Dipartimento di Ingegneria Gestionale e della Produzione, Politecnico di Torino, 10129 Turin, Italy
[3]Dipartimento di Scienza Applicata e Tecnologia, Politecnico di Torino, 10129 Turin, Italy

Corresponding author: Giuseppe Addamo (e-mail: giuseppe.addamo@ieiit.cnr.it).

ABSTRACT In this paper, a Ka/K-band antenna-feeding network in dual-circular polarization is reported. The design of the system was carried out in view of its monolithic manufacturing through selective laser melting in AlSi10Mg alloy. As a proof-of-concept for satellite telecommunication multi-beam applications, the feeding network operates in the K band (19.25, 20.75) GHz and in the Ka band (27.0, 29.0) GHz. The system provides four rectangular-waveguide ports and a common dual-polarized circular-waveguide port to be connected to the feed horn. The prototype exhibits measured values of in-band return loss better than 28 dB and a port-to-port isolation better than 19 dB (in polarization) and 50 dB (in frequency). The cross-polar discrimination is higher than 20 dB. In this regard, an elliptical-waveguide line was specifically designed and manufactured to recover a value higher than 30 dB in both frequency bands. The line can be easily integrated in the feed horn to be connected to the feeding-network thanks the ease of customization provided by 3D printing. The insertion losses are lower than 0.5 and 0.2 dB in the K and Ka bands, respectively. The weight of the prototype is approximately 130 g.

INDEX TERMS 3D-printing, additive manufacturing, antenna feeds, microwave systems, selective laser melting, and waveguide passive.

I. INTRODUCTION

In several industrial sectors, additive manufacturing is revolutionizing the way in which products are designed and manufactured thanks to the inherent advantages w.r.t. conventional machining (*e.g.*, free-form capability, near-net-shaping, reduction of material waste, and ease of customization). In the microwave field, additive manufacturing technologies have already proved to be viable solutions for the development of waveguide components exhibiting improvements in terms of performance, mechanical complexity, mass, and envelope. Among the others, single waveguide components manufactured through stereo-lithography and selective laser melting are leaky-wave antennas [1], waveguide transitions [2], [3], ortho-mode transducers and polarizers [4], [5], waveguide circuitry [6]-[8], filters [9]-[12], lightweight perforated structures [13]. The main advantage of additive manufacturing technologies is the integration of several radio-frequency functionalities (including radiation, phase-shifting, polarization and frequency diplexing) in a single mechanical part. Some examples of microwave system-integration empowered by AM are waveguide arrays with integrated waveguide filters [14], components with twisting, bending and filtering capabilities [15], horn-antennas arrays integrated with diplexers [16], arrays of single-polarization antenna-feed chains [17], microwave circuits printed on antennas [18], and complex array systems [19], [20].

Within this context, satellite telecommunication payloads are envisaged to greatly benefit from AM technologies in terms of reduction of mass, envelope, lead time/cost, and complexity of assembling/integration/testing procedures. These advantages are very evident in the development of multi-beam antenna systems for High-Throughput Satellite (HTS) platforms based on frequency-reuse schemes [21]-[23]. Indeed, both single-feed-per-beam and multi-feed-per-beam configurations ask for the development and housing in the satellite platform of hundreds of antenna-feed chains operating in dual-polarization and dual-band mode.

To the best of Authors' knowledge, the only monolithic development of these antenna-feed systems has been

This article has been accepted for publication in a future issue of this journal, but has not been fully edited. Content may change prior to final publication. Citation information: DOI 10.1109/ACCESS.2021.3089826, IEEE Access

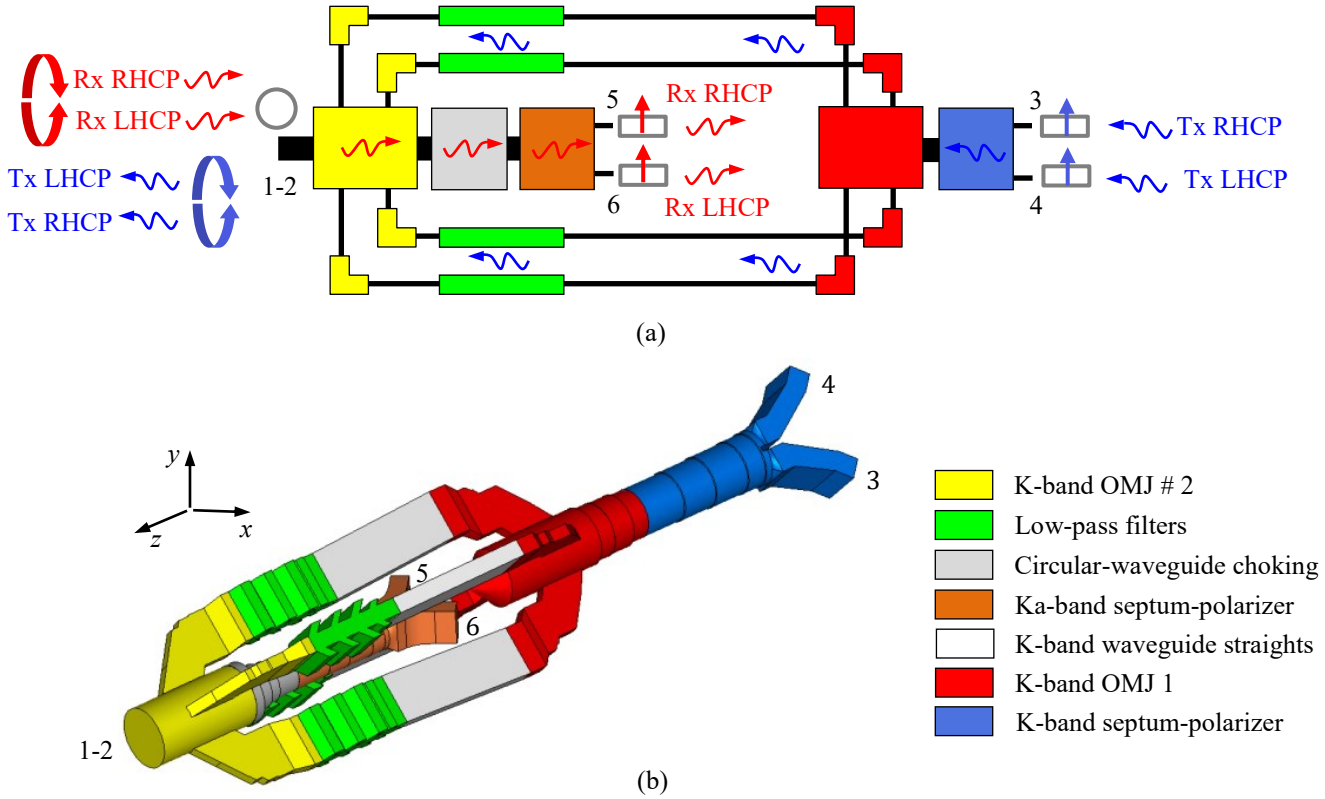

FIGURE 1. Block diagram (a) and Inner waveguide structure (b) of the K/Ka-band feeding-network optimized for additive manufacturing. Electrical ports 1 and 2 are the two polarizations at the common waveguide (V/H or RHCP/LHCP). Ports 3 and 4 are the K-band W42 ports. Ports 5 and 6 are the Ka-band WR28 waveguide ports.

reported in [17], where a dual-band antenna-feed chain working within the (10.5, 15.0) GHz frequency band and in single-linear polarization is described. The reported single-polarization architecture consists of a lower number of building blocks w.r.t fully dual-band dual-circular-polarization antenna-feed subsystems. The latter require also higher dimensional accuracy to control the amplitude and phase equalization of the channels necessary to achieve the required axial ratio. This requirement translates in a robust electromagnetic design oriented to the manufacturing process. In this work, a complete dual-band dual-circular-polarization antenna-feeding network operating in the higher frequency bands (19.25, 20.75) GHz + (27.0, 29.0) GHz is presented. All the building blocks are integrated in a single mechanical part to be connected to a feed-horn illuminating the reflector. The latter was not integrated in the feeding network in order to both accurately measure the complete scattering matrix of the system and to allow for the optimal orientation of the prototype within the available SLM machine volume (250 mm x 250mm x 200 mm). Additionally, the applicability of the SLM process to the manufacturing of high-performance feed horns operating from Ku band to V band had already been assessed in [24]. Section II describes the electromagnetic design and performance of all the building blocks and of the complete feeding network. The mechanical model and the manufacturing of the prototype are presented in Section III. Finally, in Section IV the measured performance of the prototype are compared with the simulations of the de-embedded CAD model and the recovery of the cross-polar discrimination (XPD) through an elliptical-waveguide line is described.

II. ELECTROMMAGNETIC DESIGN AND SIMULATED PERFORMANCE

The proof-of-concept of monolithic K/Ka-band dual-polarization feeding networks presented in this paper was designed to operate in (19.25, 20.75) GHz (K band) and in (27.0, 29.0) GHz (Ka band). The system had to provide the following typical requirements for HTS payloads,

- Return loss > 23 dB
- Insertion loss < 0.5 dB
- Dual circular-polarization mode
- Isolation vs polarization between ports > 20 dB
- Isolation vs frequency between ports > 50 dB
- XDP > 30 dB
- Transversal envelope within the feed-horn aperture (diameter = 35 ÷ 50 mm depending on the specific coverage scenario).

Different architectures can be considered for the implementation of dual-band dual-polarization antenna-feed chains, among which are the ones consisting of

This article has been accepted for publication in a future issue of this journal, but has not been fully edited. Content may change prior to final publication. Citation information: DOI 10.1109/ACCESS.2021.3089826, IEEE Access

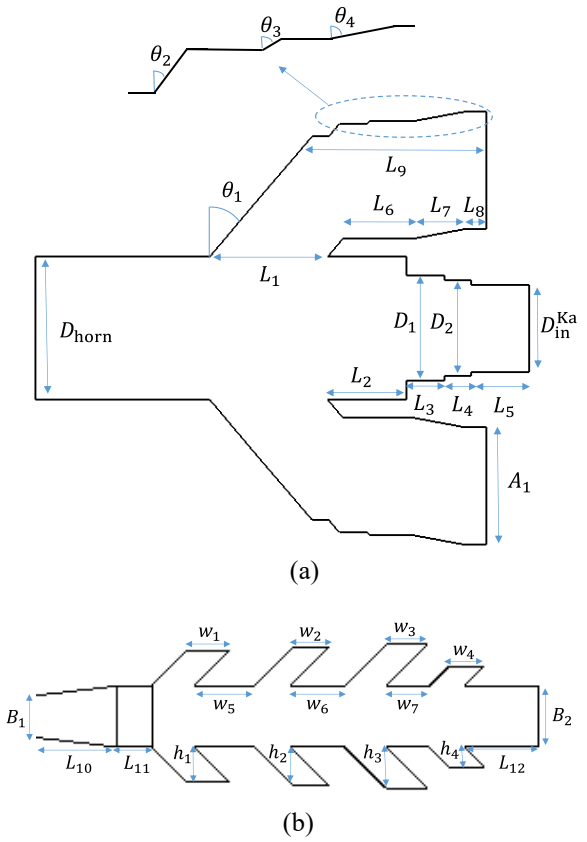

FIGURE 2. Section views of the self-diplexing ortho-mode transducer. (a) K-band ortho-mode junction OMJ #1 loaded with the circular-waveguide choking. (b) Low-pass *E*-band filter with stubs tilted by 45°.

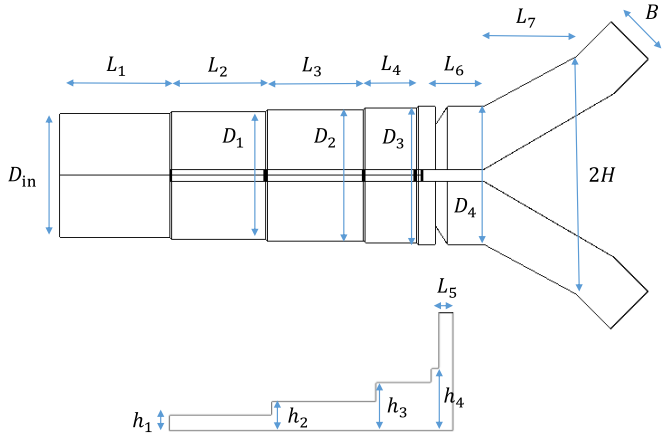

FIGURE 3. Section view of the K- and Ka-band septum polarizers with detailed view of the septum.

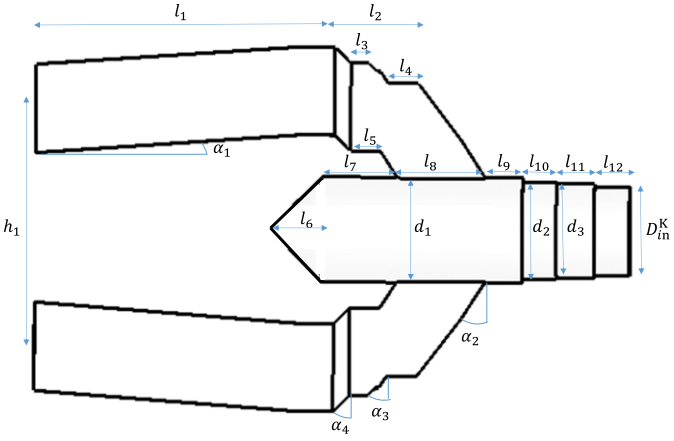

FIGURE 4. Section view of the K-band ortho-mode junction OMJ #1.

- Frequency-diplexing structures integrated along the feed-horn [25].
- High-frequency coupling slots in the first section connected to the feed-horn [26].
- Low-frequency coupling slots in the first section connected to the feed-horn [27]-[28].
- Dual-band ortho-mode junctions and polarizers [29].

In this work, the architecture presented in [28] was selected, since it allows for a streamline mechanical configuration that is particularly suitable for additive manufacturing. The dual-band dual-circular operating mode is achieved by means of two single-band septum polarizers, whose working principle is described in [30]. The block diagram and the 3D view of the inner waveguide structure of the feeding network are shown in Fig. 1, where the key building blocks are highlighted with different colors, along with the port numbering. The feeding network is to be connected to a dual-band feed-horn at the common circular port corresponding to the electrical ports 1 and 2. The latter are the two TE_{11} mode polarizations, either V/H or RHCP/LHCP, although the feeding network is designed to operate in circular polarization mode. The K-band signals enter from the WR42-waveguide ports 3 and 4 and are converted, through the K-band septum polarizer, in RHCP and LHCP signals propagating towards the first K-band ortho-mode junction (OMJ #1). The latter exhibits a two-fold symmetry and routes the two polarizations from the circular waveguide of the K-band septum polarizer to four rectangular-waveguide arms. The extracted K-band signals propagate through four low-pass filters (one per arm) and are coupled to the common circular waveguide by the second K-band ortho-mode junction (OMJ #2). This junction is loaded at one port with a circular-waveguide choking so that the coupled K-band signals propagate towards the feed-horn port. Due to the low-pass filters, the Ka-band RHCP/LHCP signals at the feed-horn port are routed to the Ka-band septum polarizer that converts these signals into two linearly polarized signals at the WR28-waveguide ports 5 and 6.

The following sub-sections describe in details the geometry and the electromagnetic performance of all the building blocks, which were specifically tailored to the SLM manufacturing. In this regard, the XPD requirement (> 30 dB) demands for a high level of both the symmetry of the

This article has been accepted for publication in a future issue of this journal, but has not been fully edited. Content may change prior to final publication. Citation information: DOI 10.1109/ACCESS.2021.3089826, IEEE Access

Table I. Comparison between designed, measured and simulated performances of the K/Ka-band feeding network.

K-BAND SCATTERING PARAMETERS			
Parameter	Design	Measurement	De-embedded simulation
S_{33} , S_{44} (dB)	≤ -30	≤ -28	≤ -30
S_{43} (dB)	≤ -22	≤ -19	≤ -22
S_{V3}/S_{H3} (dB)	0 ± 0.1	0.70 ± 0.13	0.69 ± 0.20
S_{V4}/S_{H4} (dB)	0 ± 0.1	-0.69 ± 0.18	-0.69 ± 0.08
S_{V3}/S_{H3} (deg)	-90 ± 0.2	-81.4 ± 1.5	-81.0 ± 1.3
S_{H4}/S_{4V} (deg)	-90 ± 0.2	-98.7 ± 1.2	-99.1 ± 0.9
S_{RHCP3} (dB)	≥ -0.4	≥ -0.45	≥ -0.44
S_{LHCP4} (dB)	≥ -0.4	≥ -0.49	≥ -0.44
S_{LHCP3} (dB)	≤ -40	≤ -20	≤ -20
S_{RHCP4} (dB)	≤ -40	≤ -20	≤ -20
S_{53}, S_{63} (dB)	≤ -100	≤ -100	≤ -100
S_{54}, S_{64} (dB)	≤ -100	≤ -100	≤ -100

KA-BAND PARAMETERS			
Parameter	Design	Measurement	De-embedded simulation
S_{55} , S_{66} (dB)	≤ -30	≤ -29	≤ -28
S_{65} (dB)	≤ -26	≤ -26	≤ -26
S_{V5}/S_{H5} (dB)	0 ± 0.05	0.16 ± 0.04	0.14 ± 0.04
S_{V6}/S_{H6} (dB)	0 ± 0.05	-0.16 ± 0.03	-0.17 ± 0.03
S_{V5}/S_{H5} (deg)	-90 ± 1.5	-80.8 ± 0.4	-80.5 ± 0.3
S_{H6}/S_{V6} (deg)	-90 ± 1.5	-99.1 ± 1.2	-99.4 ± 0.76
S_{RHCP5} (dB)	≥ -0.1	≥ -0.13	≥ -0.13
S_{LHCP6} (dB)	≥ -0.1	≥ -0.16	≥ -0.16
S_{LHCP5} (dB)	≤ -37	≤ -21	≤ -21
S_{RHCP6} (dB)	≤ -37	≤ -21	≤ -21
S_{53}, S_{63} (dB)	≤ -50	≤ -50	≤ -50
S_{54}, S_{64} (dB)	≤ -50	≤ -50	≤ -50

waveguide cross-sections and the equalization of the waveguide-channels lengths. As discussed in [31], these geometrical requirements are more easily guaranteed if the main propagation axis of the feeding network is aligned with the building direction. This condition implies that the components have to be designed so that all the surfaces of the internal channels are self-supporting (*i.e.,* do not require supporting structures during the 3D printing process) according to this orientation of the feeding network on the building platform.

A. SELF-DIPLEXING ORTHO-MODE TRADSUCER

The self-diplexing Ortho-Mode Transducer (OMT) is the most complex building-block of the feeding network, since it has to simultaneously provide frequency and polarization diplexing of the signals. This building block consists of the following components: the ortho-mode junction OMJ #2, the four low-pass filters, and the circular-waveguide choking. In the present design, the two K-band polarized signals are symmetrically coupled from the common circular waveguide to the four rectangular waveguides through the multi-slope L-junction presented in [31]. The propagation of the Ka-band signals in the rectangular-waveguide arms is prevented through four symmetric *E*-plane stub filters loading the L-junction. The stubs were tilted by 45° according to the design presented in [32], in order to allow for the proper orientation of the feeding network on the building platform. The Ka-band signals, instead, propagate along the common circular-waveguide channel that is connected, through the waveguide choking, to the Ka-band septum polarizer. The waveguide choking consists of a cascade of circular-waveguide steps and prevents the propagation of the K-band signals towards the Ka-band septum polarizer.

The geometry of the self-diplexing ortho-mode transducer is shown in Fig. 2, in which the geometrical variables are also defined. The diameter of the input circular-waveguide was set to D_{horn} = 12.240 mm in order to excite only the two TE_{11} modes in both bands, under a perfect two-fold

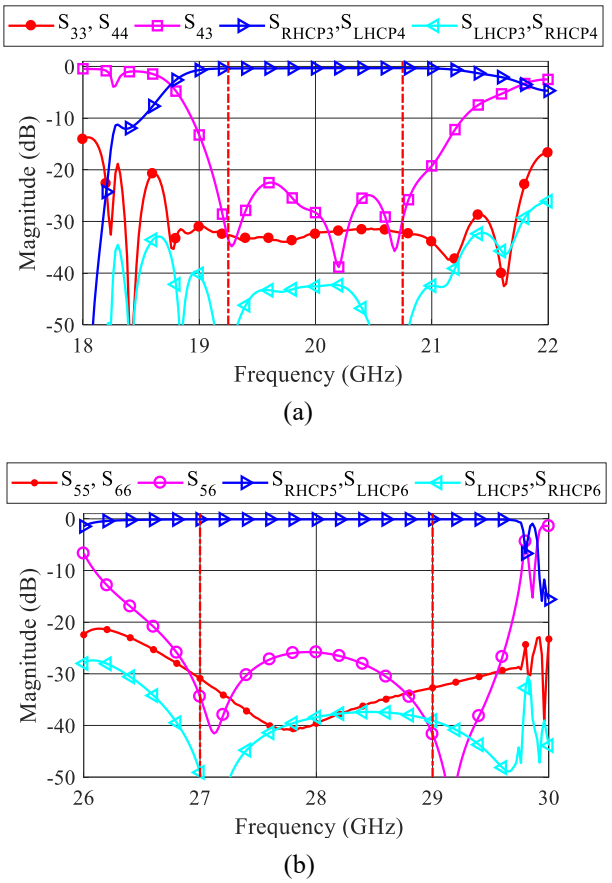

FIGURE 5. Predicted scattering coefficients of the K/Ka-band feeding network. (a) K band. (b) Ka band.

symmetry condition. On the other hand, the diameter of the output circular-waveguide of the choking connected to the Ka-band septum polarizer is D_{in}^{Ka} = 7.500 mm, corresponding to a cut-off frequency of the TE_{11} mode equal to 23.4 GHz. The values of the other geometrical parameters defined in Fig. 2 are

- L_i={10.100, 6.870, 3.200, 2.260, 5.000, 6.000, 4.380,

This article has been accepted for publication in a future issue of this journal, but has not been fully edited. Content may change prior to final publication. Citation information: DOI 10.1109/ACCESS.2021.3089826, IEEE Access

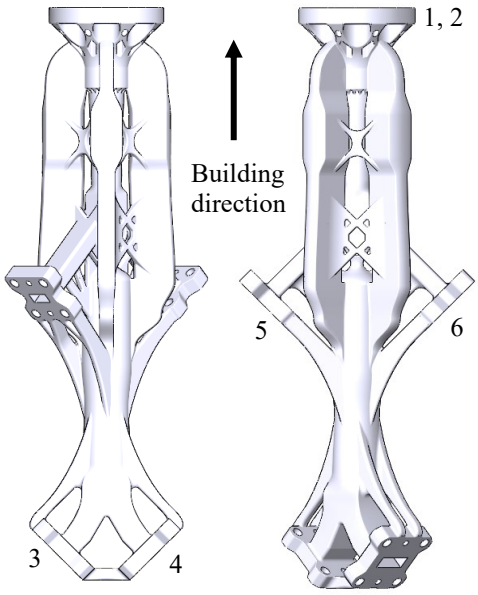

FIGURE 6. 3D views of the mechanical CAD model of the K/Ka-band feeding network of Fig. 1.

FIGURE 7. Prototype of the K/Ka-band feeding network manufactured through the selective laser melting process. (a) Prototype as built, still attached to the building platform. (b) Prototype after stress relieving, detachment, cleaning, and shot-peening.

1.910, 14.900, 4.380, 1.910, 4.000} mm,
- D_i= { 9.050, 8.260} mm,
- θ_i= { 40.00°, 40.00°, 45.00°, 79.40°},
- w_i={2.310, 3.250, 1.910, 2.970, 2.230, 2.330, 1.860} mm,
- h_i={2.740, 2.980, 3.190, 1.530}$/\sqrt{2}$ mm,
- $B_1 = 2.277$ mm, B_2=3.3 mm, and $A = 10.086$ mm.

The component exhibits an in-band return loss better than 29 dB at all ports and a port-to-port isolation in frequency better than 50 dB.

B. K- AND KA-BAND SEPTUM POLARIZERS

The K- and Ka-band septum polarizers were designed according to the layout presented in [31] that is customized for AM. As shown in Fig. 3, this geometry consists of an input circular-waveguide connected to a cascade of four circular-waveguide steps in which a septum with increasing height is inserted to introduce the 90-degree phase difference between the two linear polarizations. The ridge width is constant and equal to 1 mm. Finally, two 45-degree bends are used to achieve the sufficient clearance to accommodate standard flanges at the rectangular-waveguide ports.

With reference to Fig. 3, the values of the geometrical parameters of the K-band septum polarizer are
- D_{in}=10.100 mm,
- D_i ={10.400, 10.700, 11.000, 11.300} mm,
- h_i = { 0.850, 1.273, 1.765, 1.326} mm,
- L_i ={9.030, 7.847, 8.040, 4.260, 0.505, 1.060, 0.990, 3.267} mm;
- $H = 9.732$ mm, and $B = 4.318$ mm.

This geometry guarantees values of return loss and port-to-port isolation better than 30 dB, along with an XDP value better than 40 dB.

The Ka-band septum-polarizer is defined by the following geometrical parameters
- D_{in} =7.500 mm,
- D_i ={7.525, 7.550, 7.575, 7.600} mm,
- h_i = { 0.422, 0.985, 1.237, 0.94} mm,
- L_i ={5.005, 5.726, 2.985, 0.305, 0.766, 3.007, 2.342} mm,
- $H = 6.807$ mm, and $B = 3.556$ mm.

The corresponding performance are return loss > 30 dB, port-to-port isolation > 28 dB, and XPD > 37 dB.

C. K-BAND ORTHOMODE JUNCTION OMJ #1

As shown in Fig. 4, the geometry of the OMJ #1 used for extracting the signals from the circular waveguide of the K-band septum polarizer is similar to that of OMJ #2, except for the short-circuit loading the left circular-waveguide port. At the opposite side, the OMJ includes a cascade of circular-waveguide steps designed to achieve the input diameter of the K-band septum polarizer. In consideration of the selected orientation on the platform, the main complexity in the design of this component concerns the geometry of the short circuit in order to avoid overhanging structures that can warp or collapse during the manufacturing process,

According to the parameters labelling reported in Fig. 4, the optimized geometrical values are:
- d_i={11.754, 10.963, 10.446} mm,
- h_1= 27.088 mm,

This article has been accepted for publication in a future issue of this journal, but has not been fully edited. Content may change prior to final publication. Citation information: DOI 10.1109/ACCESS.2021.3089826, IEEE Access

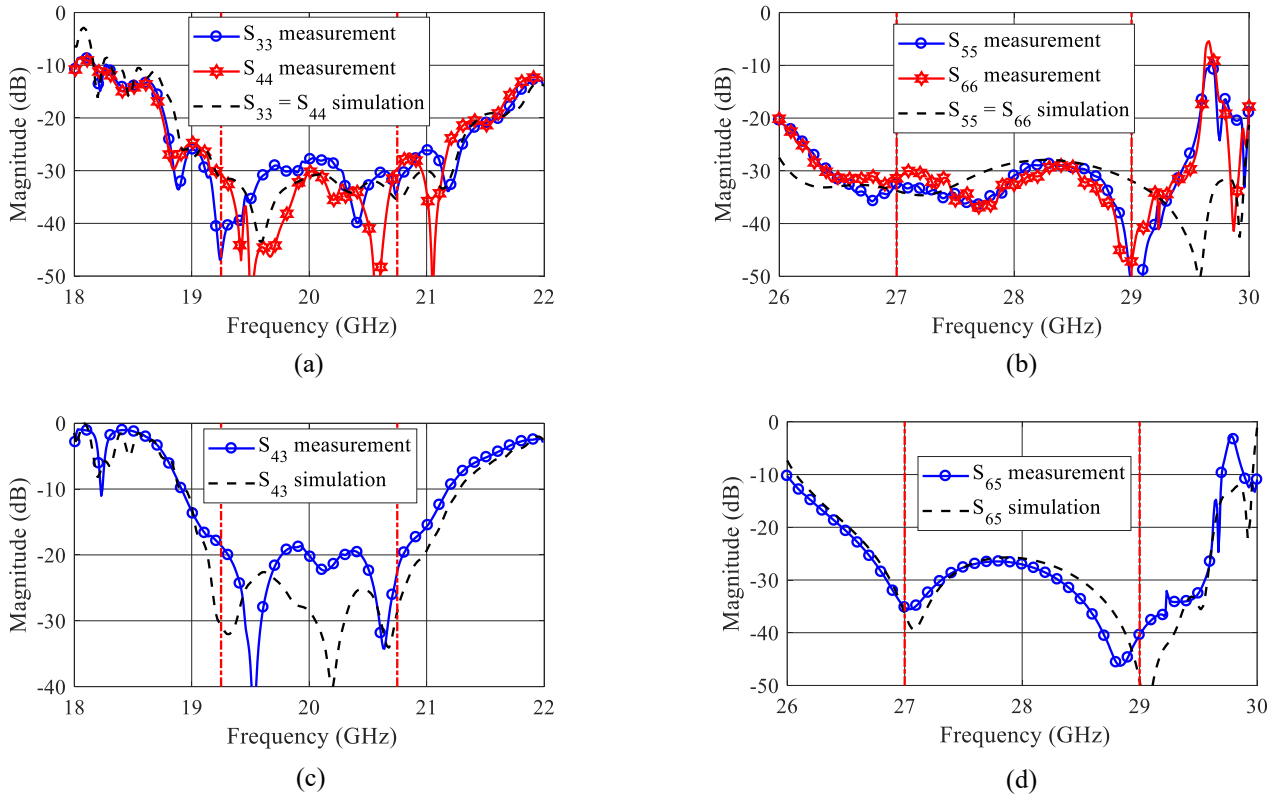

FIGURE 8. Measured and simulated scattering reflection and isolation coefficients of the K/Ka-band feeding network at the rectangular-waveguide ports. The simulated data refer to the de-embedded CAD model described in the text. (a) Reflection coefficients in K band at the WR42 ports 3 and 4. (b) Reflection coefficients in Ka band at the WR28 ports 5 and 6. (c) Isolation in K band between the WR42 ports 3 and 4. (d) Isolation in Ka band between the WR28 ports 5 and 6.

- l_i= {34.000, 9.451, 2.067, 3.432, 3.404, 5.889, 8.591, 10.017, 4.250, 3.857, 4.301, 4.000} mm, and
- α_i={3.81, 36.00, 44.00, 45.00}°.

The return loss of the designed component is higher than 28 dB

D. OVERALL RF PERFOMANCES

The in-band values of the simulated scattering coefficients of the complete feeding network of Fig. 1 are reported in Table I. The corresponding frequency responses are shown in Fig. 5. The system provides an in-band return loss level > 30 dB at all ports with a port-to-port isolation in polarization better than 22 dB in K band and 26 dB in Ka band. The isolation level is lower in K band because of the cascade of the self-diplexing OMT with the ortho-mode junction OMJ #1 that leads to a return loss > 22.4 dB for this sub-assembly. The circular polarizations excited by the K-band septum polarizer are, hence, cross-reflected according to this value. The port-to-port isolation in frequency is better than 50 dB. A very high level of XPD (> 35 dB) is guaranteed by the design in both bands.

III. MECHANICAL DESIGN AND MANUFACTURING

The mechanical CAD model of the feeding network implementing the waveguide structure of Fig. 1 is shown in Fig. 6. As previously discussed, the feeding-network geometry was conceived in view of printing the prototype along its common propagation axis through the SLM process.

The external profile of the mechanical CAD model traces the inner waveguide-channel contour with metal walls of variable thickness. The thickness was defined so as to balance several aspects. Indeed, the highly desirable minimization of weight has to be traded-off against the risk of deformations that can occur because of the friction force between the blade and the part during the spreading of the powders. As the best compromise, a thickness of 1 mm was used to build the upper part (*i.e.*, the Ka-band septum polarizer and the self-diplexing OMT), while metal walls of 2 mm thickness were used for the lower part (*i.e.*, the K-band septum polarize and the OMJ #1). This mechanical layout allows for higher rigidity and best building quality. Indeed, the lower part is connected to the platform during the printing process and, hence, has to be robust and well-

This article has been accepted for publication in a future issue of this journal, but has not been fully edited. Content may change prior to final publication. Citation information: DOI 10.1109/ACCESS.2021.3089826, IEEE Access

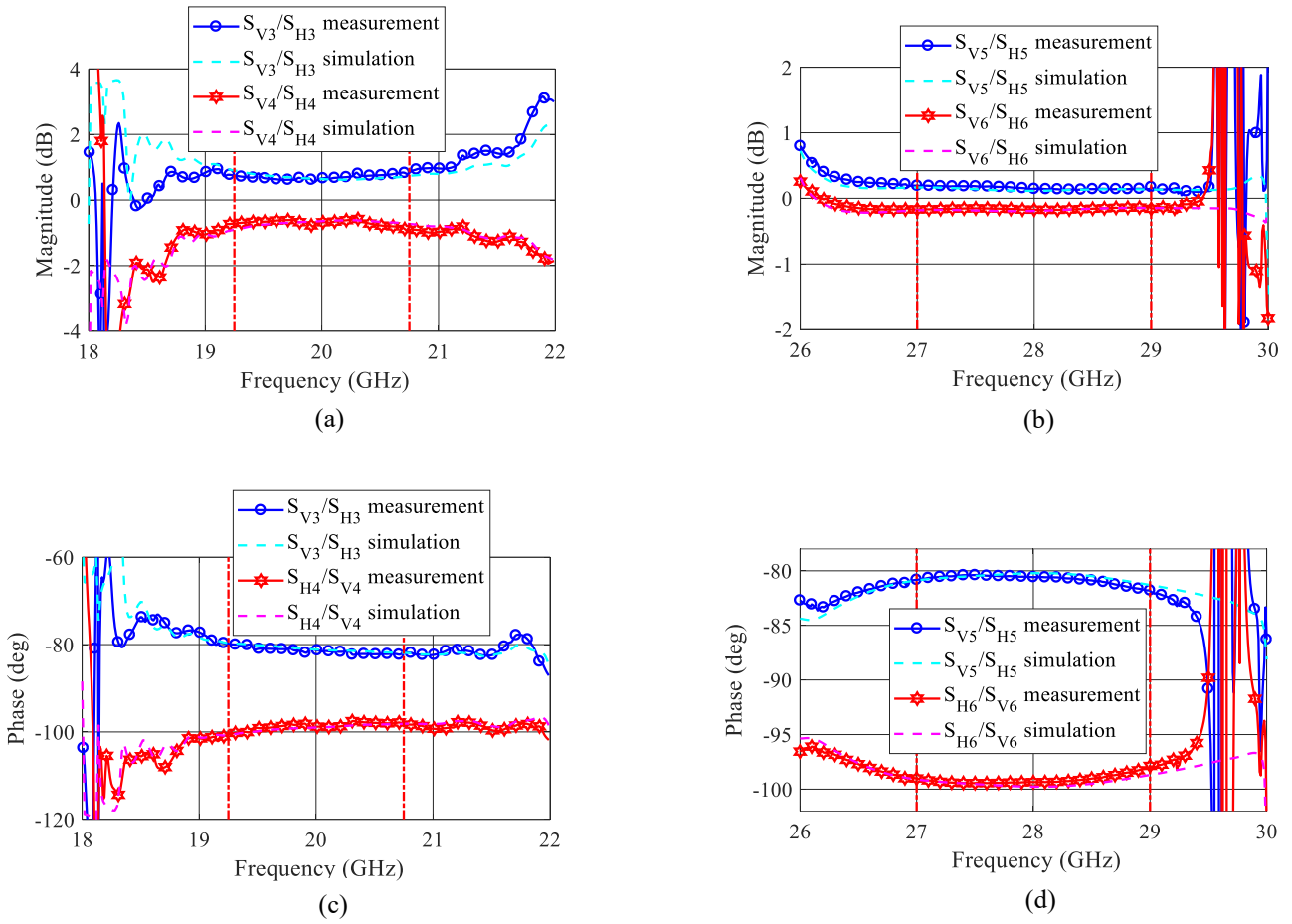

FIGURE 9. Measured and simulated unbalances between the linear-polarization transmission coefficients of the K/Ka-band feeding network. The simulated data refer to the de-embedded CAD model described in the text. (a) Amplitude unbalance between the K-band transmission coefficients from the WR42 ports 3 and 4 to the linear polarizations V and H at the circular-waveguide port. (b) Amplitude unbalance between the Ka-band transmission coefficients from the WR28 ports 5 and 6 to the linear polarizations V and H at the circular-waveguide port. (c) Phase unbalance between the K-band transmission coefficients from the WR42 ports 3 and 4 to the linear polarizations V and H at the circular-waveguide port. (d) Phase unbalance between the Ka-band transmission coefficients from the WR28 ports 5 and 6 to the linear polarizations V and H at the circular-waveguide port.

anchored to the platform, in order to avoid detachment of the prototype. In this regard, it has to be pointed out that the risk of detachment from the platform gradually grows with the height of the printed part. In order to stiffen those parts (for instance, the WR28 and WR51 flanges) that could mostly be affected by the vibrations produced by the blade movement, self-supporting ribs were inserted in the mechanical CAD model. Full ribs would had made the structure more rigid, but at expense of higher mass and center of gravity and, hence, higher instability and thermal stresses during the manufacturing process. The network of ribs was designed by taking inspiration from the ramifications of roots and branches in the trees.

Fig. 7(a) shows the prototype manufactured through the SLM process in AlSi10Mg, still attached to the building platform. Due to the selected electromagnetic and mechanical design, the 3D printing of the prototype required supporting structures only for the standard flanges at the WR42 and WR28 waveguide ports. The positions of the latter were defined in order to ease the connection to the Network-Analyzer (NA) measurement setup. For this reason, the prototype fits within a cylinder of 70-mm diameter and 180-mm length. If higher integration of the flanges is implemented in the mechanical CAD model, the envelope diameter reduces to 43 mm. A custom flange was implemented at the common circular-waveguide that provides eight M3 screw holes and eight holes for the alignment pins of diameter equal to 2 mm.

After the stress-relieving process and detachment from the platform, the prototype was cleaned and subjected to shot-peening. The stress-relieving process allows for reducing the risk of deformation and wrapping of the part when it is detached from the platform. These effects can be generated by the high stresses arisen during the high-power building process that actually melts the metal powders. Shot peening, instead, is applied to reduce the surface roughness and, hence, the equivalent surface electrical resistivity. For RF applications, asking for high dimensional

This article has been accepted for publication in a future issue of this journal, but has not been fully edited. Content may change prior to final publication. Citation information: DOI 10.1109/ACCESS.2021.3089826, IEEE Access

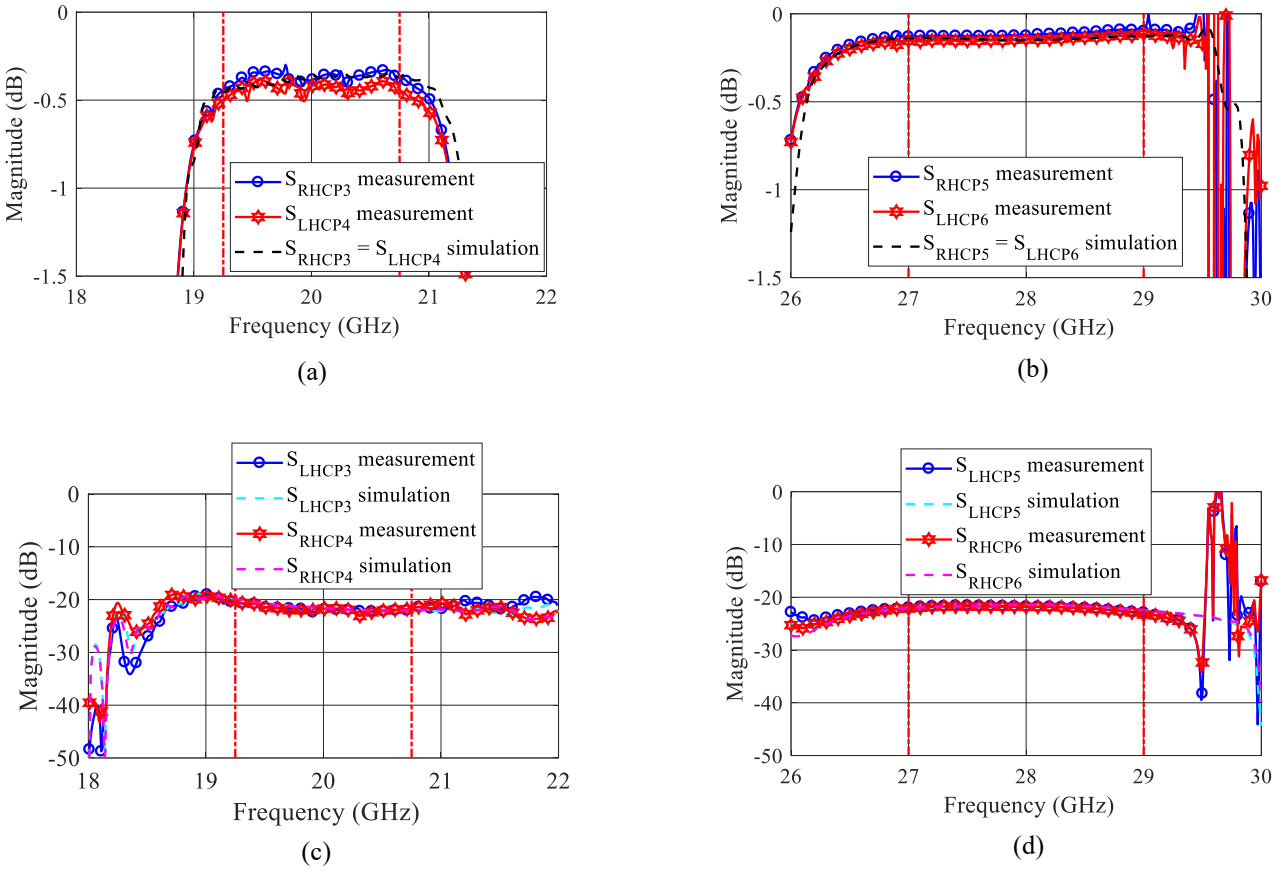

FIGURE 10. Measured and simulated scattering transmission coefficients of the K/Ka-band feeding network from the rectangular-waveguide ports to the circular polarizations LHCP and RHCP at the circular-waveguide port. The simulated data refer to the de-embedded CAD model described in the text. (a) Co-polar transmission coefficients in K band between the WR42 ports 3 and 4 to the coupled circular polarizations at the circular-waveguide port. (b) Co-polar transmission coefficients in Ka band between the WR28 ports 5 and 6 to the coupled circular polarizations at the circular-waveguide port. (c) Cross-polar transmission coefficients in K band between the WR42 ports 3 and 4 to the uncoupled circular polarizations at the circular-waveguide port (d) Cross-polar transmission coefficients in Ka band between the WR28 ports 5 and 6 to the uncoupled circular polarizations at the circular-waveguide port.

accuracy and low electrical resistivity, both post-processings are mandatory. Hence, the experimental testing was performed on the post-processed prototype. Details of the SLM manufacturing and post-processing steps are reported in [33]. The weight of the prototype is approximately 130 g. The final prototype is shown in Fig. 7(b).

III. TESTING AND MEASURED PERFORMANCE

The full dual-polarization scattering matrix of the prototype was measured in each frequency band by adopting the measurement technique described in [34]. To this aim, the relevant rectangular waveguide ports were connected to the NA, while the remaining rectangular-waveguide ports were terminated on matched loads. The circular-waveguide port was connected, in turn, to five calibration standards, *i.e.* a matched load, a short circuit, the short circuit shifted back by a circular-waveguide line, a diagonal reactive load, and the latter standard shifted back by the circular-waveguide line. The main advantage of this technique compared to the adapter-removal one is that the two polarizations at the circular waveguide are considered at the same time, avoiding artifacts caused by spurious reflections of the polarization not coupled to the waveguide adapter.

Direct measurement of the scattering transmission coefficients between the WR42 and WR28 ports was also carried out in Ka band, in order to assess the isolation provided by the low-pass filters. In this case, an adapter from WR42 to WR28 flanges was used to connect the NA to each WR42 port. The isolation in K band was verified to be higher than the NA dynamic range (100 dB). In all the measurements the NA was calibrated via the thru-reflection-line technique.

A. K/KA-BAND FEEDING NETWORK

For due comparison with the designed performances, the measured scattering parameters of the K/Ka-band feeding network are summarized in Table I.

This article has been accepted for publication in a future issue of this journal, but has not been fully edited. Content may change prior to final publication. Citation information: DOI 10.1109/ACCESS.2021.3089826, IEEE Access

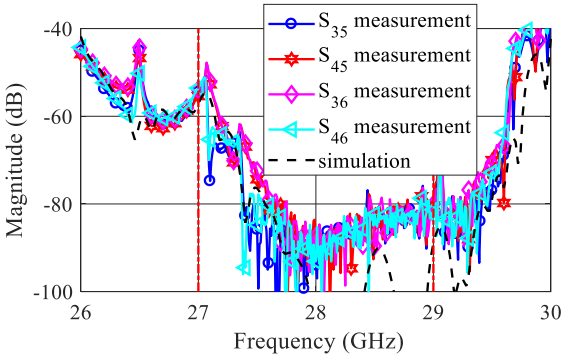

FIGURE 11. Measured and simulated Ka-band transmission coefficients between the WR42 and WR28 waveguide ports of the K/Ka-band feeding network. The simulated data refer to the de-embedded CAD model described in the text.

Although an overall fair agreement was achieved between the designed and measured performances, significant deviations occurred in the equalization between the scattering transmission coefficients from the rectangular-waveguide ports to the linear H and V-polarized TE_{11} modes propagating in the common circular waveguide. The amplitude and phase unbalances lead, in both frequency bands, to spurious excitation of the uncoupled circular polarizations in the order of -20 dB. These unbalances are caused by asymmetries of the long circular-waveguide sections of the polarizers and combiners.

In order to evaluate these dimensional errors, the measured unbalances were reconstructed by considering elliptical-waveguide sections in the CAD model. The principal directions of the elliptical waveguides were rotated with respect to the reference H and V-polarizations of the feeding network (*i.e.*, *x* and *y* axes in Fig.1).

The performance of the de-embedded CAD model are summarized in Table I, whereas Fig. 8 - Fig. 11 compare the performance over frequency of the de-embedded CAD model against the measured responses. The tight agreement between the measured and simulated frequency responses assures that the CAD model of the manufactured prototype was properly de-embedded. Specifically, the circular-waveguide sections of the K-band polarizer and of the K-band OMJ #1 were replaced by elliptical waveguide sections with principal axes of ± 0.04 mm w.r.t the nominal diameters. The principal directions were rotated by +16° w.r.t. to the V-H reference basis of the feeding network, being the ellipses minor direction +16° apart from the H-pol. direction. The Ka-band transmission unbalances were reproduced by introducing in the Ka-band polarizer the same type of error. In this case, the principal directions were rotated by +3° and the corresponding axes are ± 0.046 mm w.r.t the nominal diameters. It follows that the dimensional accuracy achieved in the SLM manufacturing of the entire prototype are better than 0.05 mm. This value is fairly comparable with the one that is achievable in the

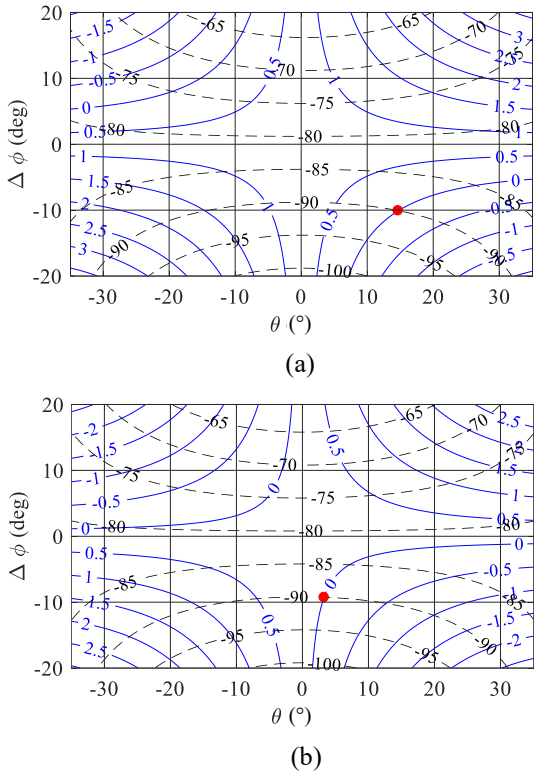

FIGURE 12. Amplitude (blue solid lines) (dB) and phase (black dashed lines) (deg) contour plots of the linear-transmission-coefficients ratio of the prototype cascaded with an ideal rotated elliptical-waveguide line. The red dots denote the elliptical-waveguide parameters for single-band compensation (reported in the text). (a) $S_{V,3}/S_{H,3}$ (K band). (b) $S_{V,5}/S_{H,5}$ (Ka band).

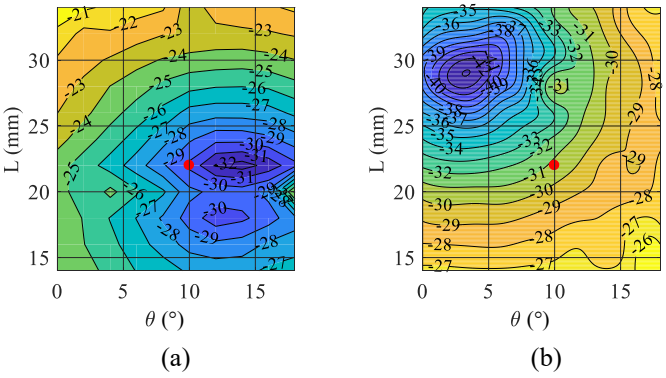

FIGURE 13. Contour maps of the simulated performance of the K/Ka-band feeding network as a function of the length L and rotation angle θ of an elliptical-waveguide line connected to its circular waveguide port. The major and minor axes of the elliptical waveguide are d_x = 12.440 mm and d_y = 12.040 mm, respectively. The red dot refers to the manufactured elliptical waveguide line. (a) Maximum cross-polar transmission coefficient in K band. (b) Maximum cross-polar transmission coefficient in Ka band.

electrical discharge machining of long parts (>100 mm) with undercuts. In the following Sub-section IV.B, a method to fully recover the transmission unbalances is presented.

This article has been accepted for publication in a future issue of this journal, but has not been fully edited. Content may change prior to final publication. Citation information: DOI 10.1109/ACCESS.2021.3089826, IEEE Access

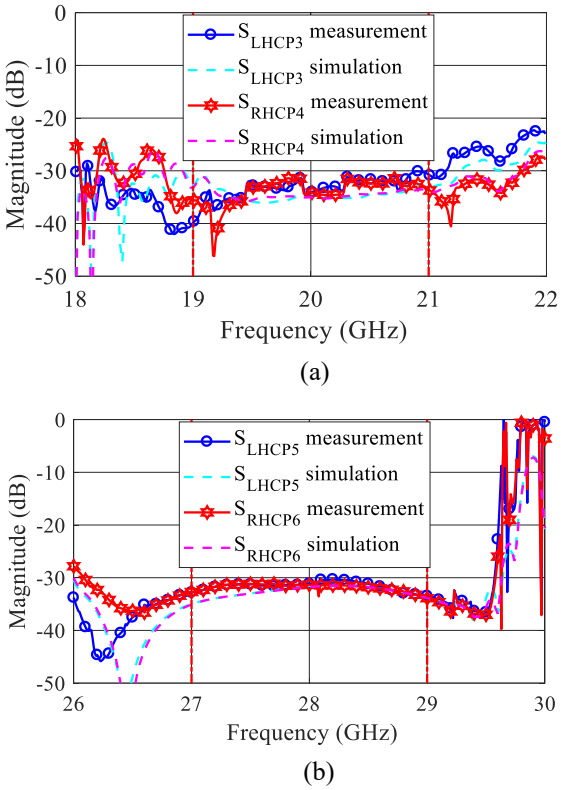

FIGURE 14. Measured and simulated cross-polar transmission coefficients of the K/Ka-band feeding network cascaded with the compensation elliptical waveguide at the circular-waveguide port. (a) Cross-polar transmission coefficients in K band from the WR42 ports 3 and 4 to the uncoupled circular polarizations at the circular waveguide port. (b) Cross-polar transmission coefficients in Ka band from the WR28 ports 5 and 6 to the uncoupled circular polarizations at the circular waveguide port.

B. K/KA- BAND FEEDING NETWORK WITH COMPENSATION ELLIPTICAL-WAVEGUIDE LINE

In order to properly recover the amplitude and phase equalization between the linear-polarization transmission coefficients of the K/Ka-band feeding network, an elliptical-waveguide line can be connected to the circular-waveguide port of the breadboard. To this end, the two scattering transmission sub-matrices of the prototype (with the measured in-band values reported in Table I)

$$\boldsymbol{S}_{\mathrm{VH},34} = \begin{bmatrix} S_{\mathrm{H3}} & S_{\mathrm{H4}} \\ S_{\mathrm{V3}} & S_{\mathrm{V4}} \end{bmatrix} \text{ and } \boldsymbol{S}_{\mathrm{VH},56} = \begin{bmatrix} S_{\mathrm{H5}} & S_{\mathrm{H6}} \\ S_{\mathrm{V5}} & S_{\mathrm{V6}} \end{bmatrix}$$

can be, in turn, cascaded with the scattering transmission sub-matrix of an ideal elliptical-waveguide line.

The latter submatrix is

$$\boldsymbol{S} = \begin{bmatrix} \mathrm{S_{HH}} & \mathrm{S_{HV}} \\ \mathrm{S_{VH}} & \mathrm{S_{VV}} \end{bmatrix}$$

with elements

$$S_{\mathrm{HH}} = e^{j\varphi}(1 + e^{j\Delta\varphi}\sin^2\theta - \sin^2\theta)$$
$$S_{\mathrm{HV}} = S_{\mathrm{VH}} = e^{j\varphi}\sin 2\theta\,(e^{j\Delta\varphi} - 1)/2$$
$$S_{\mathrm{VV}} = e^{j\varphi}(e^{j\Delta\varphi} + \sin^2\theta - e^{j\Delta\varphi}\sin^2\theta),$$

where φ is the common phase-delay, $\Delta\varphi$ is the phase-delay difference between the two principal axes x and y, and θ is the rotation angle between the x-y principal-axes system and the V-H reference system of the feeding network.

The ratios $S_{\mathrm{V,3}}/S_{\mathrm{H,3}}$ and $S_{\mathrm{V,5}}/S_{\mathrm{H,5}}$ between the resulting linear transmission-coefficients are plotted in Fig. 12 as a function of the elliptical-waveguide parameters $\Delta\varphi$ and θ. As denoted by the red dots in Fig. 12, nearly ideal compensation can be achieved in each single band through the following elliptical-waveguide parameters

- K-band: $\Delta\varphi$ = -9.8 deg , θ = 14.2°
- Ka-band: $\Delta\varphi$ = -9.3 deg , θ = 3.3°.

Since the optimum values of the rotation angle θ are different for the two bands and the nearly equal values of $\Delta\varphi$ can only be implemented through different lengths L of the compensation line (because of frequency dispersion), a sub-optimum compensation elliptical-waveguide line had to be defined.

To this end, the spurious cross-polar transmission coefficients of the prototype cascaded with the compensation line were computed as a function of the geometrical parameters θ and L. Full-wave simulations of the scattering matrix of the elliptical-waveguide line were carried out in order to also consider the additional reflection arising at the interface between the circular and elliptical waveguides. The principle axes were set to d_x = 12.440 mm and d_y = 12.040 mm so as to keep the additional reflection below -30 dB in both frequency bands. Fig. 13 shows the contour maps of the simulated cross-polar transmission coefficients of the prototype cascade with the line as a function of the length L and rotation angle θ. The red dot indicates the geometry of the elliptical-waveguide line (θ = 10°, L = 22 mm) that minimizes the cross-polar transmission coefficients in both bands (< -30 dB).

An elliptical-waveguide line with these values was manufactured and the scattering parameters of the K/Ka-band feeding network connected to the line were measured. As expected, the measured cross-polar transmission coefficients (shown in Fig. 14) are better than -30 dB. These values correspond to amplitude and phase equalization better than 0.35 dB and 3 deg in both frequency bands, respectively.

Fig. 15 shows the measured and simulated residual unbalances between the linear-polarization transmission coefficients. These results confirm the validity of the recovery strategy. The effects of the elliptical-waveguide line on the other scattering parameters were measured to be negligible. It has to be highlighted that the compensation elliptical-waveguide line can be integrated in the input section of the feed horn to be mounted at the circular-waveguide port of the K/Ka-band feeding network, thus avoiding the use of additional mechanical parts and fully exploiting the ease-of-customization capability of AM processes.

This article has been accepted for publication in a future issue of this journal, but has not been fully edited. Content may change prior to final publication. Citation information: DOI 10.1109/ACCESS.2021.3089826, IEEE Access

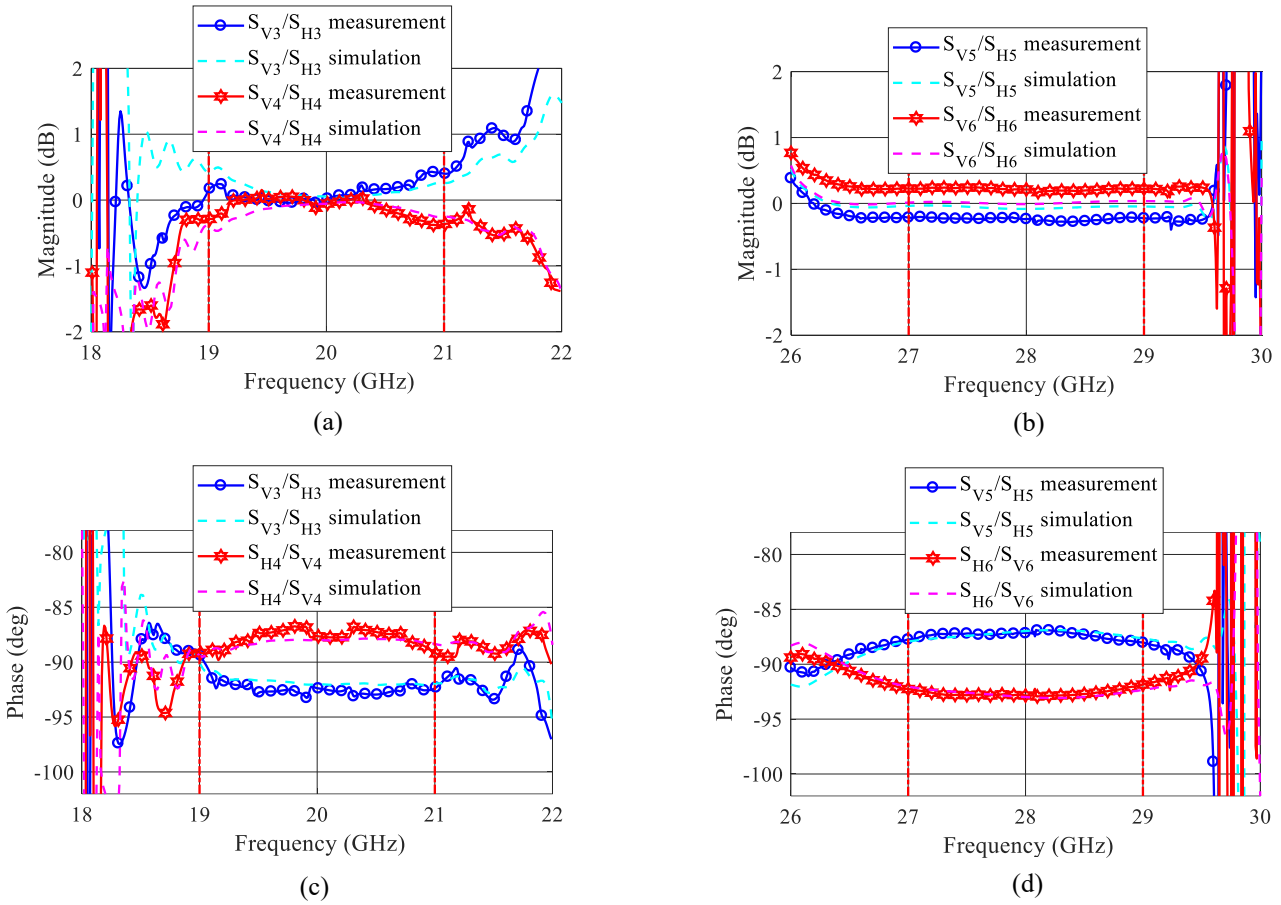

FIGURE 15. Measured and simulated unbalances between the linear-polarization transmission coefficients of the K/Ka-band feeding network cascaded with the compensation elliptical-waveguide at the circular-waveguide port. (a) Amplitude unbalance between the K-band transmission coefficients from the WR42 ports 3 and 4 to the linear polarizations V and H at the circular-waveguide port. (b) Amplitude unbalance between the Ka-band transmission coefficients from the WR28 ports 5 and 6 to the linear polarizations V and H at the circular-waveguide port. (c) Phase unbalance between the K-band transmission coefficients from the WR42 ports 3 and 4 to the linear polarizations V and H at the circular-waveguide port. (d) Phase unbalance between the Ka-band transmission coefficients from the WR28 ports 5 and 6 to the linear polarizations V and H at the circular-waveguide port.

IV. CONCLUSION

In this work, for the first time, the monolithic additive manufacturing of a complete K/Ka-band antenna-feeding network operating in dual-circular polarization has been demonstrated. The electromagnetic performance of the prototype are in line with typical requirements set for satellite telecommunication antenna systems. A strategy for recovering the spurious effects caused by the SLM dimensional tolerances has also been reported.

REFERENCES

[1] M. García-Vigueras, E. Menargues, T. Debogovic, E. de Rijk, and J. R. Mosig, "Cost-effective dual-polarised leaky-wave antennas enabled by three-dimensional printing," *IET Microw., Antennas Propag.*, vol. 11, no. 14, pp. 1985-1991, Nov. 2017, doi: 10.1049/iet-map.2016.0950.

[2] C. Guo *et al*., "A 3-D printed E-plane waveguide magic-T using air-filled coax-to-waveguide transitions," *IEEE Trans. Microw. Theory Techn.*, vol. 67, no. 12, pp. 4984-4994, Dec. 2019, doi: 10.1109/TMTT.2019.2944355.

[3] J. Wu, C. Wang, and Y. Guo, "Ridged waveguide magic tees based on 3-D printing technology," *IEEE Trans. Microw. Theory Techn.*, vol. 68, no. 10, pp. 4267-4275, Oct. 2020, doi: 10.1109/TMTT.2020.3006570.

[4] M. Kilian, C. Hartwanger, M. Schneider, and M. Hatzenbichler, "Waveguide components for space applications manufactured by additive manufacturing technology," *IET Microw. Antennas Propag.*, vol. 11, no. 14, pp. 1949-1954, Nov. 2017, doi: 10.1049/iet-map.2016.0984.

[5] J. R. Montejo-Garai, J. A. Ruiz-Cruz, and J. M. Rebollar, "Evaluation of additive manufacturing techniques applied to a waveguide mode transducer," *IEEE Trans. Compon.Packag. Manuf. Technol.*, vol. 10, no. 5, pp. 887-894, May 2020, doi: 10.1109/TCPMT.2020.2982735.

[6] K. Glatre, L. Hildebrand, E. Charbonneau, J. Perrin, and E. Amyotte, "Paving the way for higher-volume cost-effective space antennas: Designing for manufacturing, assembly, integration, and test," *IEEE Antennas Propag. Mag.*, vol. 61, no. 5, pp. 47-53, Oct. 2019, doi: 10.1109/MAP.2019.2932313.

[7] P. Booth, J. Gilmore, E. V. Lluch, and M. Harvey, "Enhancements to satellite feed chain performance, testing and lead-times using additive manufacturing," in *10th Eur. Conf. Antennas Propag. (EuCAP)*, Davos, Switzerland, 2016, pp. 1-5, doi: 10.1109/EuCAP.2016.7481882.

[8] P. Booth, R. Roberts, M. Szymkiewicz, and C. Hartwanger, "Using additive manufacturing for feed chain and other passive microwave components," in *Proc. 11th Eur. Conf. Antennas Propag. (EuCAP)*,

Paris, France, 2017, pp. 558-562, doi: 10.23919/EuCAP.2017.7928730.

[9] R. Dahle, P. Laforge, and J. Kuhling, "3-D printed customizable inserts for waveguide filter design at X-band," *IEEE Microw. Wireless Compon. Lett.*, vol. 27, no. 12, pp. 1080-1082, Dec. 2017, doi: 10.1109/LMWC.2017.2754345.

[10] D. Miek, S. Simmich, F. Kamrath, and M. Höft, "Additive manufacturing of E-plane cut dual-mode X-band waveguide filters with mixed topologies," *IEEE Trans. Microw. Theory Techn.*, vol. 68, no. 6, pp. 2097-2107, Jun. 2020, doi: 10.1109/TMTT.2020.2981057.

[11] E. López-Oliver and C. Tomassoni, "3-D-printed dual-mode filter using an ellipsoidal cavity with asymmetric responses," *IEEE Microw. Wireless Compon. Lett.*, Mar. 2021, doi: 10.1109/LMWC.2021.3064244.

[12] C. Tomassoni, O. A. Peverini, G. Venanzoni, G. Addamo, F. Paonessa, and G. Virone, "3D Printing of microwave and millimeter-wave filters: Additive manufacturing technologies applied in the development of high-performance filters with novel topologies," *IEEE Microw. Mag*, vol. 21, no. 6, pp. 24-45, Jun. 2020, doi: 10.1109/MMM.2020.2979153.

[13] T. Chio, G. Huang, and S. Zhou, "Application of direct metal laser sintering to waveguide-based passive microwave components, antennas, and antenna arrays," *Proc. IEEE*, vol. 105, no. 4, pp. 632-644, Apr. 2017, doi: 10.1109/JPROC.2016.2617870.

[14] H. K. Mouthaan and T. Chio, "A 3D printed Ku-band waveguide array with integrated waveguide filter," in *Proc. 2019 Int. Radar Conf. (RADAR)*, Toulon, France, Sept. 2019, pp. 1-5, doi: 10.1109/RADAR41533.2019.171404.

[15] O. A. Peverini *et al*., "Integration of an H-plane bend, a twist, and a filter in Ku/K-band through additive manufacturing," *IEEE Trans. Microw. Theory Techn.*, vol. 66, no. 5, pp. 2210-2219, May 2018, doi: 10.1109/TMTT.2018.2809505.

[16] F. L. Borgne, G. Cochet, J. Haumant, D. Diedhiou, K. Donnart, and A. Manchec, "An integrated monobloc 3D printed front-end in Ku-band," in *49th Eur. Microw. Conf. (EuMC)*, Paris, France, Oct. 2019, pp. 786-789, doi: 10.23919/EuMC.2019.8910891.

[17] M. Kilian, A. Schinagl-Weiß, A. Sommer, C. Hartwanger, and M. Schneider, "Ku-band SFB-cluster manufactured by additive manufacturing techniques," in *13th Eur. Conf. Antennas Propag. (EuCAP)*, Krakow, Poland, June 2019, pp. 1-4.

[18] X. He, Y. Fang, R. A. Bahr, and M. M. Tentzeris, "RF systems on antenna (SoA): a novel integration approach enabled by additive manufacturing," in *Proc. 2020 IEEE/MTT-S Int. Microw. Symp. (IMS)*, Los Angeles, CA, USA, Oct. 2020, pp. 1157-1160, doi: 10.1109/IMS30576.2020.9223793.

[19] B. Zhang, R. Li, L. Wu, H. Sun, and Y. Guo, "A highly integrated 3-D printed metallic K-band passive front end as the unit cell in a large array for satellite communication," *IEEE Antennas Wireless Propag. Letts*, vol. 17, no. 11, pp. 2046-2050, Nov. 2018, doi: 10.1109/LAWP.2018.2824298.

[20] S.-H. Shin *et al*., "Polymer-based 3-D printed Ku-Band steerable phased-array antenna subsystem," in *IEEE Access*, vol. 7, pp. 106662-106673, 2019, doi: 10.1109/ACCESS.2019.2932431.

[21] H. Wolf, M. Schneider, S. Stirland, and D. Scouarnec, "Satellite multibeam antennas at Airbus Defense and Space," in *Proc. 8th Eur. Conf. Antennas Propag. (EuCAP)*, The Hague, The Netherlands, Apr. 2014, pp. 182-185, doi: 10.1109/EuCAP.2014.6901722.

[22] U. Hong, M. Schneider, and R. Gehring, "Slim Ka-band triple band polariser network for user and gateway antenna feed application," in *Proc. 47th Eur. Microw. Conf. (EuMC)*, Nuremberg, Germany, Oct. 2017, pp. 1163-1166, doi: 10.23919/EuMC.2017.8231055.

[23] J. Hill *et al.* "Multibeam antenna architectures for flexible capacity allocation", in *Proc. 39th ESA Antenna Workshop*, Noordwijk, The Netherlands, Oct. 2018.

[24] G. Addamo *et al.*, "3D printing of high-performance feed horns from Ku to V bands", *IEEE Antennas Wireless Propag. Lett.*, vol. 17, no 11, pp. 2036-2040, Nov. 2018, doi: 10.1109/LAWP.2018.2859828.

[25] C. Granet *et al*., "The designing, manufacturing, and testing of a dual-band feed system for the Parkes radio telescope," *IEEE Antennas Propag. Mag.*, vol. 47, no. 3, pp. 13-19, Jun. 2005, doi: 10.1109/MAP.2005.1532537.

[26] R. Ravanelli *et al*., "C band self diplexed Tx/Rx feed system for telecom," in *2020 14th Eur. Conf. Antennas Propag. (EuCAP)*, Copenhagen, Denmark, Mar. 2020, pp. 1-4, doi: 10.23919/EuCAP48036.2020.9135295.

[27] M. Beadle, R. Chugh, D. Geen, S. Patel, R. Schwerdtferger, and S. Casey, "A C/X/Ku-band dual polarized Cassegrain antenna system," in Proc. *IEEE Antennas Propag. Soc. Int. Symp. 1999 Digest.*, Orlando, FL, USA, Jul. 1999, pp. 692-695, doi: 10.1109/APS.1999.789232.

[28] J. Teniente, I. Gómez-López, R. Caballero-Nagore, G. Crespo-López, and A. Martínez-Agoües, "Quad band X/Ka horn antenna and feed chain designs," in *Proc. 11th Eur. Conf. Antennas Propag. (EuCAP)*, Paris, France, Mar. 2017, pp. 3432-3436, doi: 10.23919/EuCAP.2017.7928428.

[29] R. Roberts, P. Booth, G. Fox, S. Stirland, and M. Simeoni, "Q/V-band feed system development," in *Proc. 10th Eur. Conf on Antennas Prop (EuCAP)*, Davos, Switzerland, Apr 2016, pp. 1-5, doi: 10.1109/EuCAP.2016.7481185.

[30] J. Uher, J. Bornemann, and Uwe Rosenberg, "Polarization discrimination components and equipment," in *Waveguide Components for Antenna Feed Systems*, Ist ed. Boston, USA,: Artech House Inc, 1993, pp. 371–440.ISBN: 9780890065822.

[31] G. Addamo *et al*., "Additive manufacturing of Ka-band dual-polarization waveguide components," *IEEE Trans. Microw. Theory Techn.*, vol. 66, no. 8, pp. 3589-3596, Aug. 2018, doi: 10.1109/TMTT.2018.2854187.

[32] O. A. Peverini *et al.*, "Additive manufacturing of Ku/K-band waveguide filters: A comparative analysis among selective-laser melting and stereo-lithography", *IET Microw. Antennas Propagat.*, vol. 11, no 14, pp. 1936-1942, Nov. 2017. doi: 10.1049/iet-map.2017.0151.

[33] F. Calignano, O. A. Peverini, G. Addamo, and L. Iuliano, "Accuracy of complex internal channels produced by laser powder bed fusion process", *Journal of Manufact. Processes*, vol. 54, pp. 48-53, Jun. 2020, doi: doi.org/10.1016/j.jmapro.2020.02.045.

[34] O. A. Peverini, R. Tascone, A. Olivieri, M. Baralis, R. Orta, and G. Virone, "A microwave measurement procedure for a full characterization of ortho-mode transducers", *IEEE Trans. Microw. Theory Tech.*, vol. 51, no 4, pp. 1207 -1213, April 2003. doi: 10.1109/TMTT.2003.809629.